crystals

MDPI

Article

Regional Thermal Cycles, Microstructure, and Local Mechanical Properties of U75V Rail Joints Produced by Electroslag Welding

Shengfu Yu [1,*], Junjie Ni [1,2], Haitao Lin [1], Zhenyu Yu [1,*] and Fangbin Deng [1]

[1] State Key Laboratory of Materials Processing and Die & Mould Technology, Huazhong University of Science and Technology, 1037 Luoyu Road, Wuhan 430074, China; d202387030@hust.edu.cn (J.N.); d202380420@hust.edu.cn (H.L.); d202280425@hust.edu.cn (F.D.)

[2] China Academy of Machinery Zhengzhou Research Institute of Mechanical Engineering Co., Ltd., Zhengzhou 450052, China

* Correspondence: yushengfu@hust.edu.cn (S.Y.); zhenyu_yu@hust.edu.cn (Z.Y.)

Abstract

Rails are critical load-bearing components in railway transportation systems, and the quality of their welded joints is essential to operational safety. However, the large variation in rail cross-sectional geometry makes it difficult to achieve suitable thermal cycles throughout the rail base, web, and head using a uniform welding heat input. In this study, a region-specific electroslag welding strategy was developed for U75V rail, in which the rail base was welded simultaneously using three wires, while the rail web and head were welded using a single wire. Under this region-specific welding configuration, the calculated t8/5 values were 101.4, 73.6, and 62.5 s in the rail base, web, and head, respectively. Representative microstructural observations showed lamellar pearlite as a major constituent at the examined locations in all three regions. From the rail base to the head, the EBSD orientation-domain size decreased from 15.6 to 7.6 μm, and the pearlite interlamellar spacing decreased from 158.9 to 110.3 nm. These microstructural variations were accompanied by an increase in the local weld-metal ultimate tensile strength from 1130.7 to 1180.6 MPa and in hardness from approximately 33 to 36 HRC. The results reveal clear associations among the region-specific welding conditions, thermal histories, microstructural characteristics, and local mechanical properties.

Keywords: U75V rail steel; electroslag welding; microstructural evolution; interlamellar spacing; mechanical properties

1. Introduction

U75V steel is a pearlitic eutectoid steel characterized by high strength, excellent wear resistance, and favorable comprehensive mechanical properties, making it an important material for railway rails [1,2]. Its mechanical and wear properties are closely associated with the pearlitic microstructure; therefore, maintaining a predominantly pearlitic microstructure is important for welded U75V rail joints. With increasing train speeds and axle loads, welded joints represent critical regions in rail structures, and their strength, toughness, and in-service reliability are directly related to operational safety [3]. Therefore, the fabrication of U75V rail welded joints with a favorable strength–toughness balance and reliable service performance has become an important research topic in the field of railway construction and maintenance [4].

U75V steel has a carbon content of 0.75–0.80 wt.%, and the welding thermal cycle can readily induce austenite grain coarsening and nonequilibrium phase transformations [5].

Check for updates

Academic Editor: Shouxun Ji

Received: 8 September 2026
Revised: 29 September 2026
Accepted: 29 September 2026
Published: 30 September 2026

Copyright: © 2026 by the authors. Licensee MDPI, Basel, Switzerland. This article is an open access article distributed under the terms and conditions of the Creative Commons Attribution (CC BY) license.

Under rapid cooling conditions, the diffusional decomposition of austenite may be suppressed, increasing the tendency for the formation of hard and brittle martensite in the weld metal and heat-affected zone, resulting in reduced joint toughness and increased susceptibility to cold cracking [6]. Therefore, controlling the cooling process to promote pearlitic transformation while suppressing martensitic transformation is particularly important for U75V eutectoid rail steel. Moreover, a rail consists of the head, web, and base, which differ considerably in cross-sectional dimensions, thermal capacity, and heat dissipation conditions. Consequently, these regions experience distinct thermal cycles during welding, making it difficult to obtain favorable pearlitic transformation conditions throughout the entire rail section using a uniform thermal input [7]. Therefore, appropriate control of the welding thermal process according to the thermal characteristics of different rail regions is essential for regulating austenite decomposition and obtaining a predominantly pearlitic welded joint.

Currently, the principal methods used for rail welding include thermite welding, flash-butt welding, and gas-pressure welding [8]. Thermite welding requires relatively simple equipment and offers high adaptability to field conditions, whereas flash-butt welding and gas-pressure welding provide advantages such as a high degree of automation and high welding efficiency [9,10]. Nevertheless, these methods still face challenges associated with welding thermal-cycle control and undesirable phase transformation. Electroslag welding is characterized by a high and stable heat input, a large molten pool, and a relatively low cooling rate, which may reduce the hardening tendency of U75V rail joints and favor diffusional austenite decomposition and pearlitic transformation, making electroslag welding a promising alternative for producing high-quality U75V rail joints [11].

However, owing to the complex cross-sectional geometry of rails, the rail head, web, and base experience pronounced differences in local heat input and heat dissipation during electroslag welding, which can lead to significantly different cooling behaviors and austenite transformation paths in different regions [12]. Notably, Ref. [12] reported that pearlitic microstructures were retained at t8/5 values of 75–120 s, whereas a bainite–pearlite mixed microstructure appeared when t8/5 decreased to approximately 62 s, indicating that the transformation behavior is particularly sensitive in this cooling regime. Therefore, appropriate regulation of the local heat input is required to coordinate the thermal cycles across the rail section and maintain favorable conditions for pearlitic transformation. Existing studies on electroslag-welded U75V rail joints have primarily focused on overall joint performance, whereas comparatively limited attention has been devoted to the relationship between region-dependent thermal cycles and phase-transformation behavior. Khan et al. [13] employed three-wire electroslag welding to join pearlitic rails and found that the joint microstructure consisted predominantly of ferrite and pearlite. Coarse prior-austenite grains and pearlite colonies were observed near the fusion boundary as a result of the welding thermal cycle, indicating a close relationship between thermal history and microstructural evolution. Previous studies [14,15] have further demonstrated that the peak temperature and cooling rate during the welding thermal cycle are key factors governing austenite decomposition and the resulting microstructure. Variations in cooling rate affect not only the austenite transformation path but also the ferrite morphology, grain size, and crystallographic characteristics. Therefore, the relationships among region-dependent welding conditions, thermal histories, austenite decomposition, and pearlitic microstructure evolution in rail joints with complex cross-sections require further systematic investigation.

To improve the performance of electroslag-welded rail joints, previous studies have primarily focused on compositional modification and optimization of the welding thermal process [16,17]. For example, Ti addition can promote the precipitation of fine carbides and refine the pearlitic microstructure, thereby improving the strength and toughness of

the weld metal. Regulation of the temperature field and cooling process can directly affect austenite decomposition and the formation and refinement of pearlite. In addition, alloying elements can regulate the formation of ferrite, pearlite, and bainite by altering the kinetics of austenite decomposition, carbon diffusion behavior, and the thermodynamic driving force for phase transformation [18,19]. These findings indicate that the welding thermal cycle and material composition jointly govern the phase transformation and pearlitic microstructure evolution of rail welded joints. However, how region-specific welding conditions are associated with pearlite-dominated transformation and microstructural refinement across different rail sections remains to be clarified.

In this study, a region-specific consumable-nozzle electroslag welding strategy was developed for U75V eutectoid rails, with three-wire welding employed for the rail base and single-wire welding for the rail web and head. Combined with heat extraction through the water-cooled copper mold, this welding configuration was designed to generate region-dependent thermal histories in the rail base, web, and head. Numerical simulation was used to characterize the temperature fields and cooling histories, while OM, SEM, EBSD, and TEM were employed to characterize the corresponding microstructures. Particular attention was paid to the relationships among the regional welding conditions, thermal histories, EBSD orientation-domain size, pearlite interlamellar spacing, and local mechanical properties. This study aims to clarify the relationships among region-dependent welding conditions, thermal histories, microstructural evolution, and local mechanical properties of U75V rail electroslag welds.

2. Materials and Methods

2.1. Materials

U75V rail steel was selected as the base material because it is a widely used pearlitic rail steel with high strength and wear resistance, and the designation and general chemical-composition requirements of U75V rail steel are specified in GB/T 2585-2021 [20]. A self-developed FLUX-980 flux-cored wire with a diameter of 2.5 mm was employed as the welding consumable. The wire was designed with relatively high C, Mn, V, and Ti contents to compensate for dilution during electroslag welding and to facilitate the formation of a high-strength pearlitic weld metal. A consumable nozzle fabricated from Chinese grade 10 steel, with inner and outer diameters of 4 and 10 mm, respectively, was used to ensure stable current conduction and continuous melting during the consumable-nozzle electroslag welding process. A self-developed HJ-431-type flux was employed because HJ-431 flux is commonly applicable to electroslag welding and provides the electrically conductive slag pool required for stable heat generation during the process [21]. The nominal chemical compositions of the U75V rail steel, FLUX-980 flux-cored wire, and consumable nozzle used in the present study are summarized in Table 1, while the nominal composition of the self-developed HJ-431-type flux is given in Table 2.

Table 1. Nominal chemical compositions of the U75V rail steel, FLUX-980 flux-cored wire, and consumable nozzle used in this study (wt.%).

Element	C	Si	Mn	V	Ti	P	S
U75V	0.75–0.80	0.55–0.65	0.90–1.0	≤0.15	-	≤0.03	≤0.03
Flux-cored wire	1.50–1.75	0.35–0.40	1.50–1.80	≤0.50	≤0.10	≤0.03	≤0.03
Consumable nozzle	≤0.15	0.15–0.25	1.20–1.50	-	-	≤0.03	≤0.03

The rail dimensions, welding principle, and welding procedure are illustrated in Figure 1. A region-specific consumable-nozzle electroslag welding process was employed, with three-wire welding for the rail base and single-wire welding for the rail web and

head. The rail dimensions and the principle of the welding process are illustrated in Figures 1a and 1b, respectively. Before welding, the assembly gap between the two rail sections was set to 20 mm. At the beginning of welding, arcs were simultaneously initiated using the three welding wires and their corresponding consumable nozzles, designated as Nos. 1, 2, and 3. After a stable electroslag welding stage was established, the rail base was welded first. Subsequently, consumable nozzles Nos. 1 and 3 were de-energized, while the central consumable nozzle, No. 2, remained in operation to complete the welding of the rail web and head. During welding of the rail head, consumable nozzle No. 2 was reciprocally oscillated at a speed of 1.5 mm/s until the welding process was completed. The welding voltage and current used for the rail base were 32–34 V and 320–325 A, respectively, whereas those used for the rail web and head were 30–32 V and 310–320 A, respectively. Photographs of the welding process are shown in Figure 1c,d.

Table 2. Nominal chemical composition of the self-developed HJ-431-type flux used in this study (wt.%).

Powder	MnO	SiO_2	CaF_2	CaO	Al_2O_3	MgO	FeO
Content	12–15	16–20	15–20	15–25	≤10	10–15	≤1.8

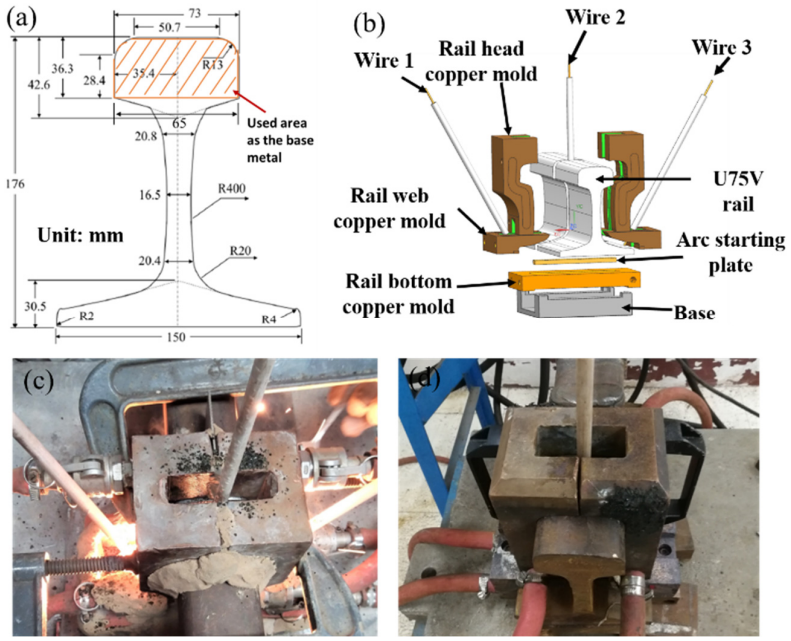


Figure 1. Schematic diagram of the three-wire consumable-nozzle electroslag welding process for U75V rails and the welding procedure: (**a**) rail cross-sectional dimensions; (**b**) schematic of the welding principle; (**c**) three-wire welding of the rail base; (**d**) single-wire welding of the rail web and head.

2.2. Microstructural Characterization

Specimens were extracted from different regions of the electroslag-welded joint for microstructural characterization. The specimens were mechanically ground, polished, and etched with a 4 vol.% nitric acid–ethanol solution. The microstructures were examined using a Motic AE2000MET optical microscope. Pearlite morphology was characterized by field-emission scanning electron microscopy (FESEM), while EBSD was used to analyze orientation, domain size, and crystallographic texture. EBSD measurements were performed with a 0.5 μm step size over a 600 × 500-pixel mapping area. The indexing success rate was approximately 94.2%. The EBSD data were used to characterize the crystallographic

orientation and orientation-domain size of the weld metal. A Tecnai G2 F30 field-emission transmission electron microscope (TEM) was employed to examine the fine microstructure and second-phase particles and to measure the pearlite interlamellar spacing. TEM specimens for interlamellar-spacing measurements were extracted from representative weld-metal regions of the rail base, web, and head. The spacing values were measured from lamellar pearlite fields in which the ferrite/cementite lamellae were clearly resolved. Because the apparent spacing can be affected by the observation-plane orientation and projection effects, the reported values are used primarily for relative comparison among the three regions.

2.3. Thermal-Field Simulation and Experimental Validation

A three-dimensional finite-element model of the U75V rail joint was established according to the actual rail geometry to simulate the transient temperature field during electroslag welding. A nonuniform hexahedral mesh was adopted to balance computational accuracy and efficiency [22,23]. The weld metal and adjacent HAZ were locally refined with a characteristic element size of approximately 1.5 mm, whereas the mesh size was gradually increased to approximately 5 mm in regions away from the weld.

The thermal loading was applied according to the actual welding sequence. During welding of the rail base, three simultaneous heat inputs corresponding to the three-wire process were applied, whereas a single heat input corresponding to the central wire was used for welding of the rail web and head. The corresponding welding parameters were 32–34 V and 320–325 A for the rail base and 30–32 V and 310–320 A for the rail web and head. Temperature-dependent thermophysical properties of U75V steel were considered. Convective and radiative heat losses were applied to the exposed rail surfaces, while enhanced heat extraction at the rail–mold interface was imposed to account for the cooling effect of the water-cooled copper mold [24]. The analysis was performed as a transient thermal simulation; therefore, no mechanical loading or displacement constraints were applied. Representative monitoring points were selected in the rail base, web, and head to obtain the temperature-time histories and determine the corresponding $t_{8/5}$ values.

The numerical model was validated by comparing the simulated thermal cycles with experimentally measured temperature histories. During electroslag welding and subsequent cooling, the surface temperatures at representative positions in the rail base, web, and head were continuously monitored using an infrared thermal imaging system. The experimental measurement positions were selected to correspond as closely as possible to the monitoring locations used in the finite-element model. The temperature–time histories obtained from the three regions were then compared with the corresponding simulated curves. The validation focused on the agreement in peak temperature, the overall shape of the thermal cycle, and the cooling behavior after the heat source passed.

2.4. Mechanical Testing

Tensile specimens were extracted from the rail-base, rail-web, and rail-head weld-metal regions to evaluate the local tensile response of the weld metal. Tensile specimens were prepared and tested in accordance with GB/T 228.1-2021, Metallic Materials—Tensile Testing—Part 1: Method of Test at Room Temperature. Room temperature tensile tests were performed using a Shimadzu universal testing machine at a constant crosshead speed of 1 mm/min. Three tensile specimens were tested for each rail region, and the reported tensile properties represent the average values of the three measurements.

Rockwell hardness measurements were performed in accordance with GB/T 230.1-2018, Metallic Materials—Rockwell Hardness Test—Part 1: Test Method, using the HRC scale. The measurement points were arranged at intervals of 2 mm along the prescribed

paths from the weld metal toward the base metal. Three independent measurements were performed at each corresponding position, and the average value was used to represent the local hardness.

3. Results

3.1. Thermal Cycles

Figure 2 compares the experimentally measured and numerically simulated thermal cycles at representative locations in the rail base, web, and head. For all three positions, the simulated curves reproduce the rapid heating and subsequent continuous cooling behavior observed experimentally, and the predicted peak temperatures are in good agreement with the measured values. Slight deviations are mainly observed during the cooling stage, which can be attributed to simplifications in the thermal boundary conditions and temperature-dependent heat-transfer coefficients used in the model.

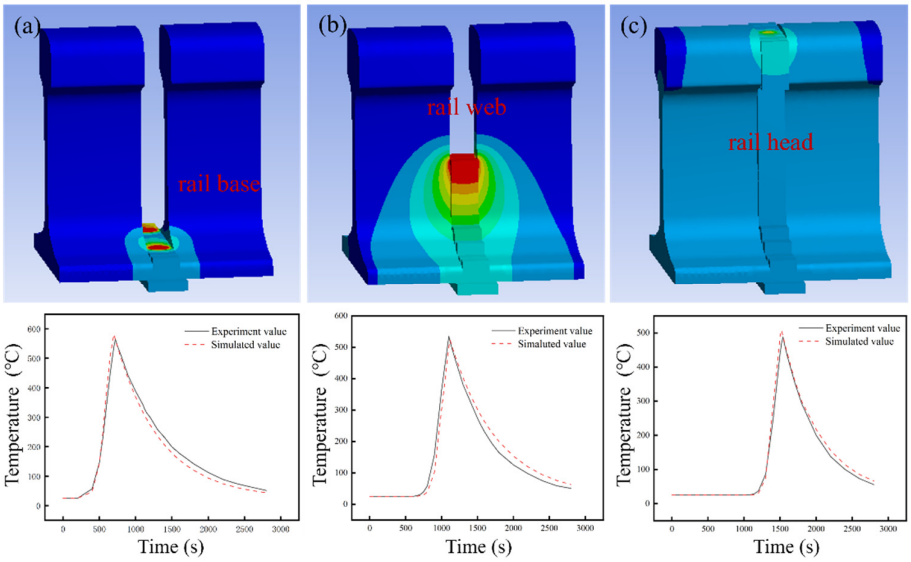


Figure 2. Simulated temperature fields and comparison between the measured and simulated thermal cycles at representative positions in the (**a**) rail base, (**b**) rail web, and (**c**) rail head.

To quantitatively evaluate the accuracy of the numerical model, the simulated and experimentally measured thermal cycles were further compared in terms of peak temperature, peak-time deviation, root-mean-square error (RMSE), and coefficient of determination (R^2). For the rail base, the experimental and simulated peak temperatures were 565.0 and 582.0 °C, respectively, corresponding to a relative error of 3.01%. The corresponding values for the rail web were 535.0 and 522.0 °C, with an error of 2.43%, while those for the rail head were 488.0 and 508.0 °C, with an error of 4.10%. The average relative error in peak temperature for the three monitoring positions was approximately 3.18%. The RMSE values for the rail base, web, and head were 22.96, 24.85, and 14.93 °C, respectively, and the corresponding R^2 values were 0.980, 0.977, and 0.992. In addition, the differences in the occurrence time of the peak temperature were approximately 20 s for all three regions. These quantitative comparisons demonstrate that the numerical model reproduces the experimentally measured transient thermal histories with reasonable accuracy and support its use for analyzing the regional thermal histories.

Figure 3 shows the simulated thermal cycles at representative locations in the rail base, web, and head under the region-specific welding conditions. Pronounced differences were observed in the cooling stage, particularly within the temperature range of 800–500 °C. The t8/5 values of the rail base welded with three wires, the rail web welded with a single wire,

and the rail head welded with a single wire were 101.4, 73.6, and 62.5 s, respectively. The corresponding nominal average cooling rates over 800–500 °C were approximately 2.96, 4.08, and 4.80 °C/s, indicating a progressive increase in cooling rate from the rail base to the rail head.

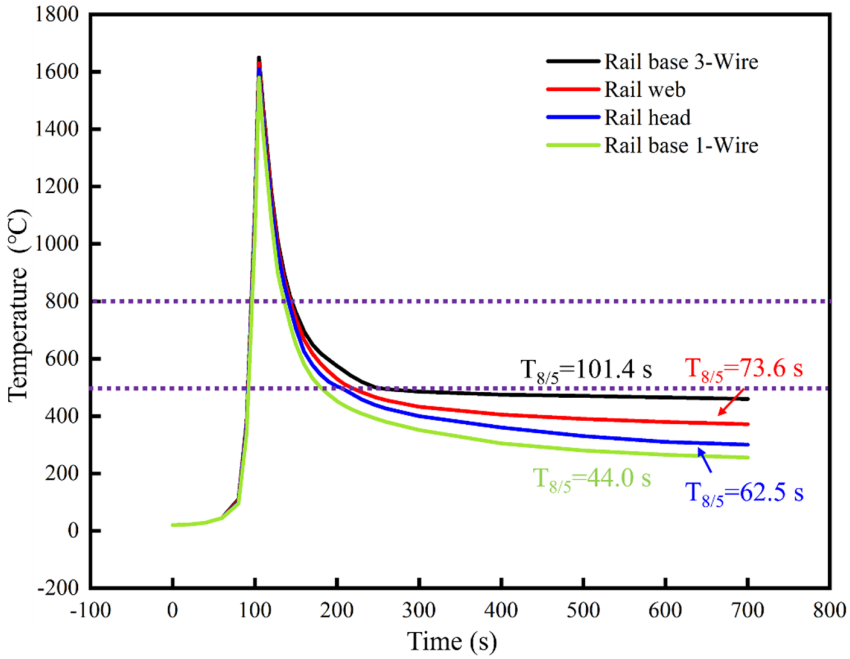


Figure 3. Simulated thermal cycles of the rail base, web, and head under region-specific welding conditions, including the comparative single-wire condition for the rail base.

To evaluate the necessity of applying three-wire welding to the rail base, a comparative thermal-cycle simulation was additionally performed using a single-wire heat input for the rail-base region. Under this condition, the t8/5 decreased markedly from 101.4 to 44.0 s, corresponding to an increase in the average cooling rate from approximately 2.96 to 6.82 °C/s. The t8/5 was therefore shortened by approximately 56.6% compared with that under three-wire welding. This result demonstrates that a single-wire heat input is insufficient to maintain a prolonged thermal cycle in the rail-base region, whereas simultaneous three-wire welding substantially increases heat accumulation and delays cooling through the transformation-sensitive temperature range.

3.2. Microstructural Evolution

Figure 4 shows the OM and SEM microstructures of the heat-affected zones in the rail base, web, and head. The OM image of the rail-base HAZ reveals distinct and relatively coarse prior-austenite grain boundaries, indicating pronounced austenite grain growth under the higher heat input and prolonged high-temperature exposure associated with three-wire welding. In contrast, the rail-web and rail-head HAZs exhibit a finer and more heterogeneous morphology, with less pronounced prior-austenite grain-boundary features, consistent with the shorter thermal exposure during single-wire welding [25,26]. Higher-magnification SEM observations revealed lamellar pearlitic morphology in the representative HAZ fields shown in Figure 4. However, because these observations represent discrete sampling areas, they are used here to characterize the local microstructural morphology rather than to establish the complete phase constitution throughout the HAZ.

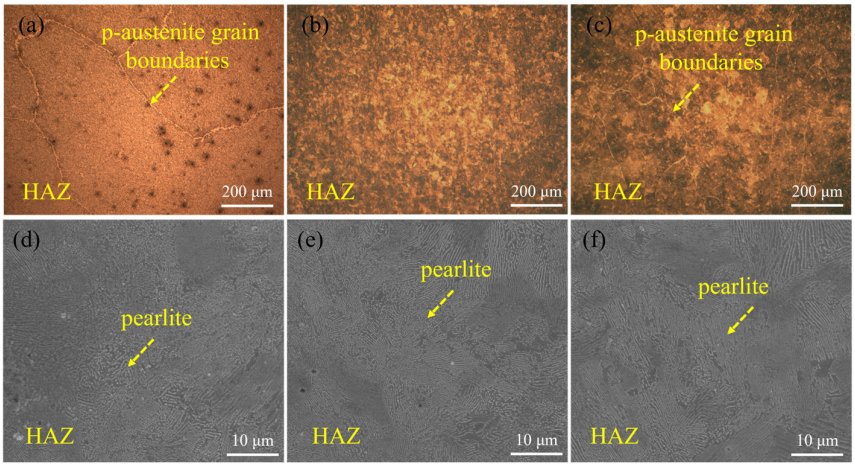


Figure 4. OM and SEM microstructures of the HAZ: (**a**,**d**) rail base; (**b**,**e**) rail web; (**c**,**f**) rail head.

Figure 5 presents the optical microstructures of the rail base, web, and head regions of the electroslag-welded U75V rail joint. As shown in Figure 5a–c, pearlitic morphology was widely observed at the representative sampling locations. No obvious martensitic constituents were identified at the optical scale. However, optical microscopy alone cannot exclude the possible presence of locally distributed bainitic constituents. Therefore, these observations are interpreted as evidence that pearlite is a major microstructural constituent at the examined locations, rather than as proof of completely pearlitic transformation throughout the entire rail section. The corresponding t8/5 values were 101.4, 73.6, and 62.5 s in the rail base, web, and head, respectively.

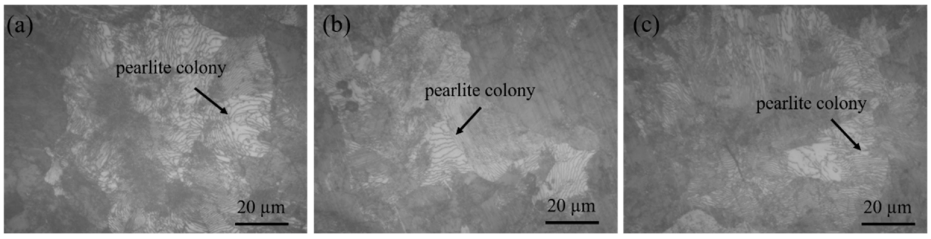


Figure 5. Microstructures of the U75V rail weld: (**a**) rail base; (**b**) rail web; and (**c**) rail head.

To further characterize the pearlitic microstructure, SEM observations were performed on the rail base, web, and head, as shown in Figure 6. Representative SEM fields in all three regions exhibited typical lamellar pearlite composed of alternating ferrite and cementite lamellae, confirming the presence of well-developed pearlitic microstructures at the examined locations.

Despite the broadly similar pearlitic morphologies observed at the examined locations, clear differences in pearlite colony morphology were observed among the three regions. The rail base exhibited relatively coarse pearlite colonies, whereas the colony size decreased through the rail web and became finer and more uniform in the rail head, as shown in Figure 6a–c. This variation is consistent with the regional thermal-cycle characteristics described above. The rail base exhibited the longest t8/5 of 101.4 s, corresponding to a comparatively prolonged thermal cycle and a coarser pearlitic morphology. After the welding process transitioned to single-wire operation, the t8/5 decreased to 73.6 s in the rail web and 62.5 s in the rail head. The progressively shorter thermal cycles corresponded to the refinement of the pearlite colonies, with the finest and most uniform morphology observed in the rail head [27,28].

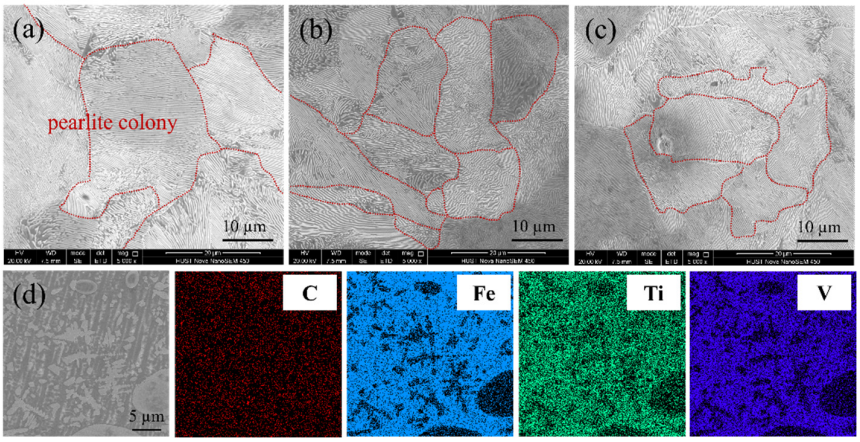


Figure 6. Pearlite colonies in the U75V rail weld: (**a**) rail base; (**b**) rail web; (**c**) rail head; and (**d**) EDS elemental maps of the rail head.

Figure 6d presents the EDS elemental maps obtained from the rail-head region. Fe, C, Ti, and V were distributed relatively uniformly within the analyzed area, and no pronounced local elemental segregation was detected within the spatial resolution of EDS. This result indicates that the observed pearlitic morphology in the rail head was not accompanied by obvious microscale elemental segregation.

Considering that the rail-head t8/5 of 62.5 s is close to the condition at which a bainite-pearlite mixed microstructure was reported in Ref. [12], additional high-magnification SEM observations were performed in the rail-head weld metal, as shown in Figure 7a–c. Well-developed lamellar pearlite is clearly visible at progressively increased magnifications. No characteristic lath-like or acicular bainitic morphology was identified within the examined field. Nevertheless, because the microstructural examination is spatially discrete, the possible presence of a small amount of locally distributed bainite at other rail-head locations cannot be completely excluded.

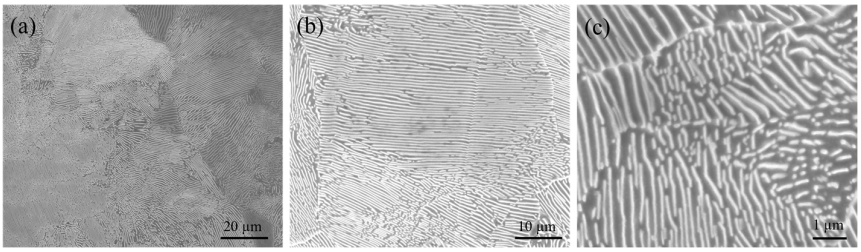


Figure 7. High-magnification SEM observations of the rail-head weld metal at progressively increased magnifications (by scale bars): (**a**) 20 μm; (**b**) 10 μm; and (**c**) 1 μm.

To further characterize the grain structures and crystallographic orientations in different regions of the weld metal, EBSD analyses were performed on the rail base, web, and head, as shown in Figure 8. As shown in Figure 8a–c, the EBSD orientation maps revealed orientation domains with different crystallographic orientations in all three weld regions. The average EBSD orientation-domain sizes were 15.6, 8.7, and 7.6 μm in the rail base, web, and head, respectively. These values describe the structural units reconstructed from the EBSD orientation data and should not be interpreted as prior-austenite grain sizes, pearlite colony sizes, or weld solidification grain sizes.

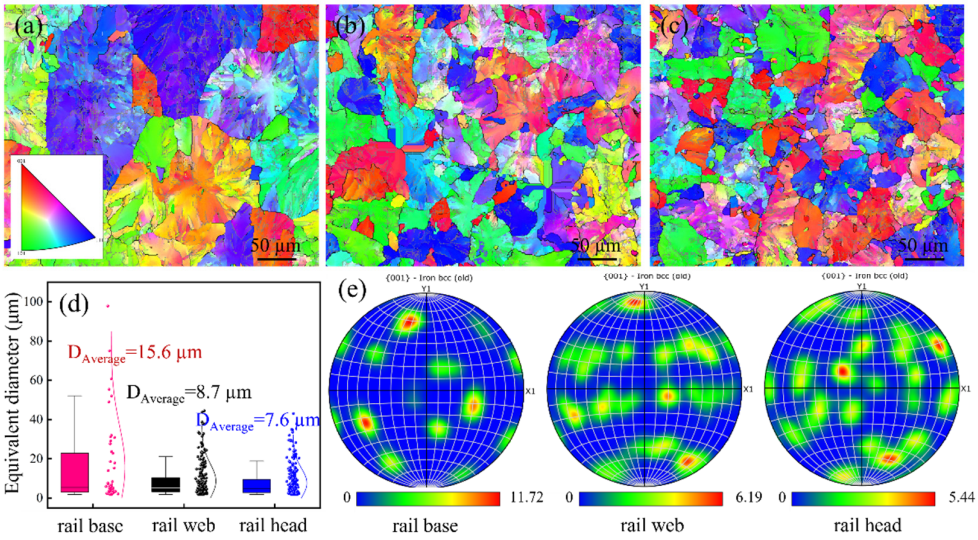


Figure 8. EBSD orientation maps and crystallographic textures of the U75V rail weld: (**a**) rail base; (**b**) rail web; (**c**) rail head; (**d**) orientation-domain size statistics; and (**e**) texture analysis.

Figure 8e presents the crystallographic orientation characteristics of the different regions. All three regions exhibited preferred crystallographic orientations, but their texture intensities differed markedly. According to the maximum orientation densities obtained from the pole figures, the maximum texture intensities in the rail base, web, and head were 11.72, 6.19, and 5.44 multiples of a uniform distribution (MUD), respectively. The rail base exhibited the highest degree of orientation concentration, whereas the crystallographic orientations in the rail web and head were more dispersed.

In the rail base, three-wire welding was associated with a higher local heat input, a larger molten pool, and longer high-temperature residence. The same region exhibited a larger EBSD orientation-domain size and stronger crystallographic texture. In comparison, the rail web and head, welded using a single wire, exhibited shorter thermal histories, smaller orientation-domain sizes, and more dispersed crystallographic orientations. These differences are interpreted as regional characteristics associated with the combined welding conditions rather than as effects of thermal history alone [29].

To further characterize the pearlite lamellar structures and nanoscale precipitates in different regions, TEM analyses were performed on the rail base, web, and head, as shown in Figure 9. Representative TEM fields from all three regions exhibited typical lamellar pearlite consisting of alternating ferrite and cementite lamellae, although their interlamellar spacings differed markedly. The mean pearlite interlamellar spacings in the rail base, web, and head were 158.9, 128.4, and 110.3 nm, respectively, demonstrating a progressive decrease from the rail base to the head.

In addition, nanoscale precipitates were observed in the weld metal, as shown in Figure 9d. The HAADF-STEM contrast and EDS results revealed that these precipitates were enriched in V and C, with measured contents of 52.05 and 38.92 wt.%, respectively, as shown in Figure 9e. The results showed that these nanoscale particles were enriched in V, while the detected C signal may also contain contributions from the surrounding matrix or specimen surface. These particles are conservatively described as V-rich precipitates. Such particles may contribute to grain-boundary pinning and resistance to dislocation motion, although their exact strengthening contribution was not quantitatively determined in the present study [30,31].

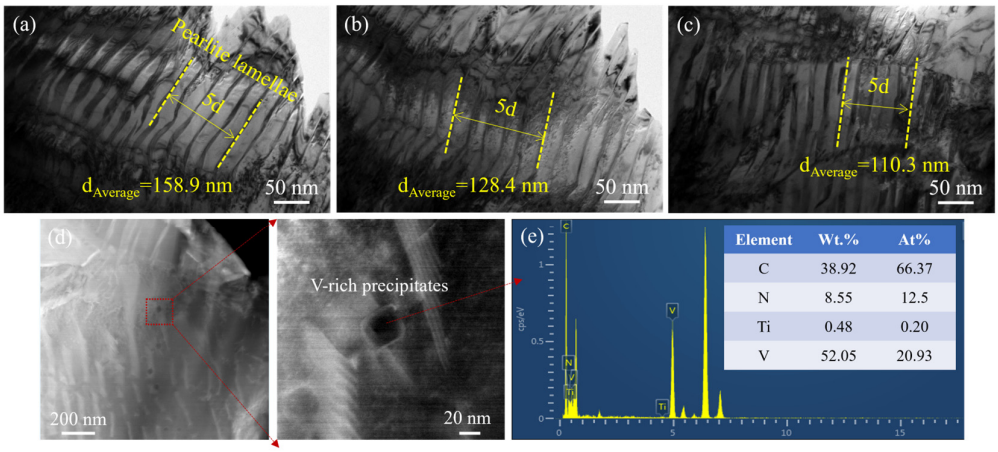


Figure 9. Pearlite interlamellar spacing and nanoscale precipitates in the U75V rail weld: (**a**) rail base; (**b**) rail web; (**c**) rail head; (**d**) V-rich precipitates; and (**e**) EDS elemental analysis.

3.3. Mechanical Properties

To evaluate the effect of regional microstructural variations on local mechanical properties, Rockwell hardness measurements were performed at the locations shown in Figure 10a. Figures 10b and 10c present the hardness distributions along the rail height and transverse to the weld, respectively.

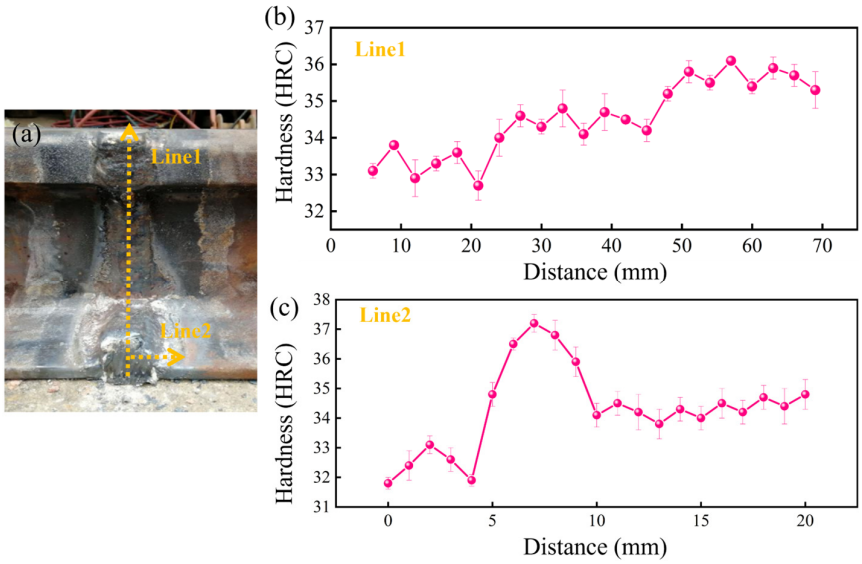


Figure 10. Rockwell hardness distributions of the U75V rail welded joint: (**a**) hardness measurement paths and the approximate peak-hardness region along Line 2; (**b**) hardness distribution along the rail height (Line 1); and (**c**) hardness distribution transverse to the weld (Line 2).

As shown in Figure 10b, the weld-metal hardness increased progressively from approximately 33 HRC in the rail base to 34–35 HRC in the rail web and approximately 36 HRC in the rail head. This variation is consistent with the regional differences in microstructural scale. From the rail base to the rail head, the EBSD orientation-domain size decreased, and the pearlite interlamellar spacing was progressively refined. Previous studies on pearlitic rail steels have shown that a reduction in pearlite interlamellar spacing increases the resistance to plastic deformation and is associated with higher strength and hardness [32,33]. In particular, Khan et al. reported that finer pearlite interlamellar spacing in electroslag-welded pearlitic rail steel resulted in increased hardness [13]. Therefore, the

higher hardness observed toward the rail-head region is associated with the finer pearlitic morphology and smaller EBSD orientation-domain size observed in that region.

As shown in Figure 10c, the hardness increased from approximately 32–33 HRC in the weld metal to above 37 HRC in the HAZ and subsequently decreased to approximately 34–35 HRC in the base metal. Taking the average weld-metal value of approximately 32.5 HRC as a reference, the local HAZ peak corresponds to an increase of approximately 13.8% in the reported HRC value. Compared with the rail-base weld metal, the reported HRC value of the rail-head weld metal increased by approximately 9.1%. This local hardening is consistent with previous studies showing that the welding thermal cycle and cooling rate can significantly modify the transformation products and pearlite morphology in the HAZ of pearlitic rail steels, resulting in pronounced local hardness variations [13]. However, because the exact peak-hardness location was not independently characterized at high magnification, the present study does not assign this increase to a specific HAZ subzone or transformation product.

Tensile tests were performed on specimens extracted from the weld-metal regions of the rail base, web, and head to compare their local tensile responses, as shown in Figure 11. The weld metal in all three regions exhibited relatively high tensile strength, although regional differences in strength and ductility were observed. The ultimate tensile strength and yield strength were 1130.7 and 776.8 MPa in the rail base, respectively, and increased to 1160.5 and 798.9 MPa in the rail web. The rail head exhibited the highest values, with an ultimate tensile strength of 1180.6 MPa and a yield strength of 805.4 MPa. In addition, the rail head exhibited the highest elongation after fracture, reaching approximately 11.5%. The relatively uniform microstructure may have contributed to reduced strain localization and favorable ductility [34].

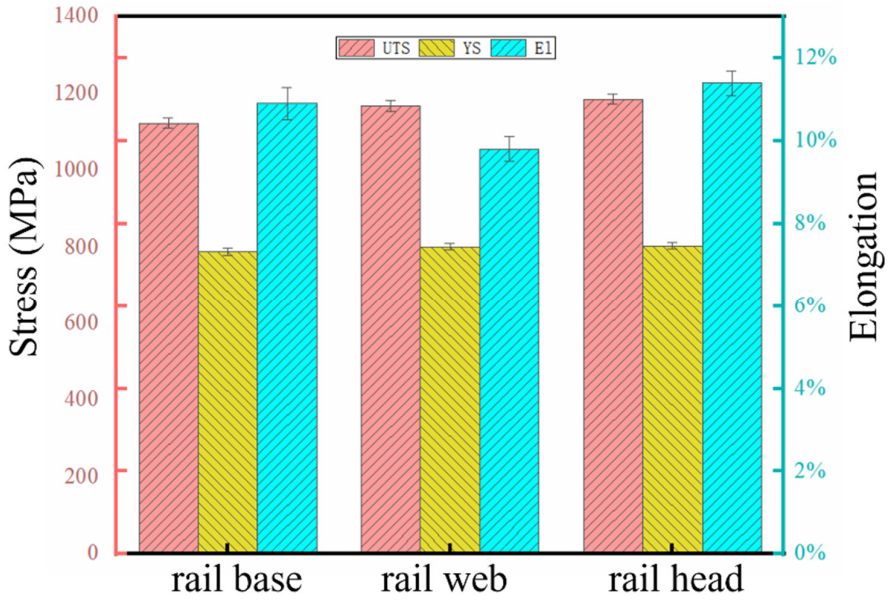


Figure 11. Local weld-metal tensile properties in the rail-base, rail-web, and rail-head regions.

Figure 12 shows the tensile fracture morphologies of the rail base, web, and head regions. The rail base exhibited relatively large flat facets and pronounced tearing ridges, indicating a comparatively limited degree of plastic deformation. In the rail web, the fracture surface became rougher and contained a greater number of small dimples, suggesting an increased contribution of ductile fracture. The rail head exhibited a large number of fine and densely distributed dimples, characteristic of a predominantly ductile fracture mode.

The progressive increase in dimple density and refinement from the rail base to the head is consistent with the improved ductility of the rail-head region.

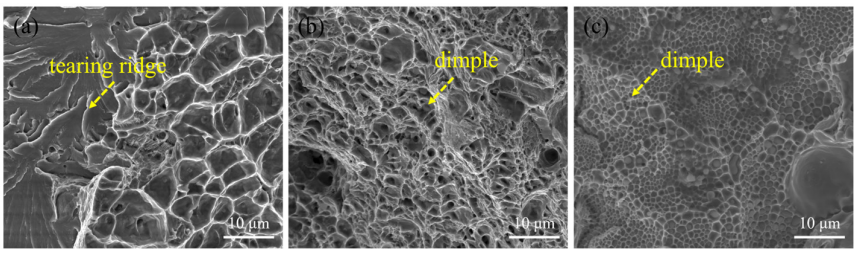


Figure 12. Tensile fracture-surface morphologies of specimens extracted from the weld-metal regions: (**a**) rail base; (**b**) rail web; and (**c**) rail head.

4. Discussion

4.1. Pearlite Transformation and Evolution of the Lamellar Structure

It should also be noted that the weld metal was formed by contributions from the U75V base metal, flux-cored wire, and consumable nozzle, which have different nominal chemical compositions. Because the welding configuration changes from three-wire/three-nozzle operation in the rail base to single-wire/single-nozzle operation in the web and head, differences in local dilution and consequently in regional weld-metal composition cannot be completely excluded. The actual bulk compositions of the rail-base, rail-web, and rail-head weld metals were not independently measured in the present study. Therefore, the observed regional differences in phase transformation, pearlite refinement, and mechanical properties should not be attributed exclusively to the thermal-cycle variation. The thermal history is considered an important contributing factor, while possible compositional effects remain a limitation of the present study.

Although the rail base, web, and head experienced different thermal cycles, representative microstructural observations showed well-developed lamellar pearlite in all three regions. These observations confirm the presence of well-developed lamellar pearlite at the examined locations. However, because the characterization was performed at discrete sampling positions, the present results do not establish the complete absence of locally distributed bainitic constituents throughout the entire welded joint. Accordingly, the following discussion focuses on the evolution and refinement of the experimentally observed pearlitic constituent.

Particular attention should be paid to the rail-head condition. The t8/5 of 62.5 s obtained in the present study is very close to the approximately 62 s condition reported in Ref. [12], where a bainite–pearlite mixed microstructure was observed. The difference of only 0.5 s in t8/5 is clearly insufficient, by itself, to account for the different microstructural observations. The t8/5 parameter represents the integrated cooling time between 800 and 500 °C and does not uniquely describe the complete thermal history of austenite. The transformation behavior can additionally be affected by the detailed cooling trajectory, peak temperature and high-temperature residence time, prior-austenite condition, local weld-metal chemistry, and observation location. In the present study, the complete calculated cooling path is provided in Figure 3, and additional high-magnification SEM examination of the rail-head weld metal revealed well-developed lamellar pearlite without characteristic bainitic morphology within the examined field. However, the bulk chemical composition of the weld metal was not independently measured. Therefore, the possible presence of localized bainite outside the examined region cannot be completely excluded. The conclusion of the present study has consequently been restricted to the directly characterized locations.

According to the Zener–Hillert theory, pearlite interlamellar spacing is controlled by the balance between the thermodynamic driving force for transformation and carbon diffusion during the cooperative growth of ferrite and cementite. The driving force for pearlite transformation originates from the Gibbs free-energy difference between austenite and the ferrite–cementite two-phase mixture [34]:

$$\Delta G_{\gamma \to \alpha + Fe_3C} = G_\gamma - G_{\alpha + Fe_3C} \quad (1)$$

It should be emphasized that Equation (1) describes the general thermodynamic basis of pearlite transformation and does not directly demonstrate a shift in the pearlite transformation temperature in the present welds. As the transformation temperature decreases, the degree of undercooling and the thermodynamic driving force increase, whereas carbon diffusivity decreases. The reduced diffusion distance restricts carbon redistribution during cooperative growth and therefore decreases the spacing between adjacent ferrite and cementite lamellae. Conversely, transformation at a higher temperature permits carbon redistribution over a longer distance and favors the formation of coarser pearlite with a larger interlamellar spacing [35,36].

The calculated $t_{8/5}$ values indicate that the cooling process became progressively faster from the rail base to the rail head, while the pearlite interlamellar spacing decreased from 158.9 to 110.3 nm. However, the start and finish temperatures of pearlite transformation were not directly measured in the present study. Therefore, the actual transformation undercooling and carbon diffusion distance cannot be quantitatively determined from the $t_{8/5}$ values alone. The observed refinement of the pearlite lamellae with decreasing $t_{8/5}$ is consistent with the possibility of transformation at a lower effective temperature, which would increase the thermodynamic driving force and reduce the effective carbon diffusion distance. This interpretation is therefore considered a plausible explanation for the observed spacing trend rather than a directly measured transformation process. Differences in the complete thermal histories, including peak temperature, high-temperature residence time, and cooling behavior outside the 800–500 °C interval, may also contribute to the regional microstructural differences.

The regional variation in pearlite colony size may also be related to differences in the prior-austenite condition. In general, longer high-temperature exposure can promote austenite grain coarsening and reduce the grain-boundary area available for heterogeneous pearlite nucleation, whereas shorter thermal exposure may favor a finer prior-austenite structure and provide more potential nucleation sites for pearlite transformation. These mechanisms provide a plausible interpretation of the observed regional differences in pearlite colony size. However, because the prior-austenite structure was not independently quantified and the regional welding conditions differed in several respects, this interpretation should not be regarded as evidence of thermal-cycle-controlled evolution [37,38].

The crystallographic texture also varied systematically among the three regions. The rail base, which experienced a longer high-temperature exposure, exhibited a stronger texture, whereas the rail web and head showed more dispersed crystallographic orientations. This trend is consistent with the possible influence of differences in high-temperature residence and orientation-selective growth, although other location-dependent welding conditions may also contribute [29].

It should be noted that the rail base, web, and head differ not only in their thermal histories but also in geometry, thermal capacity, local mold contact, molten-pool characteristics, solidification conditions, and dilution behavior. In addition, reciprocal wire oscillation was applied only during rail-head welding. Therefore, the present experimental design does not isolate the thermal cycle as an independent variable. The observed variations in EBSD orientation-domain size, pearlite interlamellar spacing, hardness, and tensile strength

should instead be regarded as regional microstructure-property differences associated with the combined welding conditions. The measured thermal histories provide an important correlation with these variations, while possible contributions from composition, high-temperature residence, solidification behavior, and other location-dependent factors cannot be excluded.

4.2. Microstructural Factors Associated with Local Mechanical Properties

The regional mechanical-property differences are discussed here in relation to the measured EBSD orientation-domain size, pearlite interlamellar spacing, and observed nanoscale precipitates. The rail base, web, and head exhibited distinct thermal histories together with region-specific microstructural characteristics and mechanical responses. These differences should be interpreted as the combined result of the regional welding conditions rather than as consequences of the thermal histories alone.

Grain size is an important microstructural factor governing the yielding behavior of metallic materials. Grain refinement increases the grain-boundary area per unit volume, thereby strengthening the barrier effect of grain boundaries against dislocation motion and increasing the yield strength. The relationship between grain size and yield strength can be described by the Hall–Petch equation [39,40]:

$$\sigma_y = \sigma_0 + k_y d^{-1/2} \quad (2)$$

where σ_y is the yield strength, σ_0 is the lattice friction stress, k_y is the Hall–Petch coefficient, and d is the average grain size. As the grain size decreases, the grain-boundary area per unit volume increases, while the length of dislocation pile-ups and the number of dislocations within each pile-up decrease. Consequently, a higher applied stress is required to transmit slip across grain boundaries and initiate plastic deformation in adjacent grains, thereby increasing the resistance of the material to yielding.

The EBSD results showed a decrease in the average orientation-domain size from the rail base to the rail head. In general, refinement of crystallographic orientation domains can increase the density of barriers to dislocation motion and may contribute to strengthening. The Hall–Petch relationship, given in Equation (2), provides a general description of grain-boundary strengthening. However, the EBSD orientation domains measured in the present study are not necessarily equivalent to prior-austenite grains, pearlite colonies, or conventional ferrite grains used in a quantitative Hall-Petch analysis. Therefore, the observed refinement is discussed here as a possible contribution to the higher rail-head strength and hardness rather than as a quantitatively demonstrated Hall-Petch strengthening mechanism.

The EBSD orientation-domain size decreased from 15.6 μm in the rail base to 7.6 μm in the rail head. This trend occurred together with the regional differences in welding conditions and thermal histories. The smaller orientation-domain size in the rail-head weld metal may provide a greater density of crystallographic barriers to dislocation motion and may therefore contribute to its higher local strength and hardness. However, because the measured orientation domains are not equivalent to conventional grains, this contribution cannot be quantitatively interpreted using the Hall–Petch relationship.

Pearlite interlamellar spacing is another important microstructural factor associated with the strength of high-carbon steels. During plastic deformation, dislocation motion within the ferrite lamellae is impeded by the ferrite–cementite interfaces. A reduction in pearlite interlamellar spacing increases the density of ferrite–cementite interfaces and shortens the effective mean free path of dislocations. Consequently, a higher applied stress

is required to sustain plastic deformation, resulting in increased strength. The relationship between pearlite interlamellar spacing and strength can be expressed as follows [41,42]:

$$\sigma_p = \sigma_0 + k_s S^{-1} \quad (3)$$

where S is the pearlite interlamellar spacing. As the interlamellar spacing decreases, the ferrite-cementite interfacial area per unit volume increases, and the effective mean free path of dislocations decreases. Consequently, a higher applied stress is required for dislocations to overcome or bypass these interfacial barriers. Therefore, refinement of the pearlite lamellar structure effectively increases the resistance of the material to plastic deformation. The progressively reduced pearlite interlamellar spacing is expected to increase the ferrite–cementite interfacial area and shorten the effective mean free path of dislocations. Together with the observed reduction in EBSD orientation-domain size, this lamellar refinement may contribute to the higher strength and hardness of the rail-head region.

It should also be noted that the local hardness peak above 37 HRC in the HAZ was not directly correlated with high-magnification SEM or EBSD characterization at the exact measurement position. Its microstructural origin therefore remains unresolved in the present study, and a possible contribution from locally formed nonequilibrium transformation products cannot be excluded.

In addition, nanoscale V-rich precipitates were observed in the weld metal. Such precipitates may exert a pinning effect on grain boundaries and may also impede dislocation motion. Therefore, they are considered a possible additional contribution to the regional strength and hardness. However, because the precipitate phase was not conclusively identified by diffraction and its number density and volume fraction were not quantified for each region, its contribution should not be regarded as an independently demonstrated strengthening mechanism [30,31].

5. Conclusions

(1) The region-specific three-wire/single-wire electroslag welding strategy resulted in distinct thermal histories in the rail base, web, and head, with t8/5 values of 101.4, 73.6, and 62.5 s, respectively.

(2) Representative observations showed lamellar pearlite as a major constituent at the examined locations in all three regions. The average EBSD orientation-domain size decreased from 15.6 to 7.6 μm, while the maximum texture intensity decreased from 11.72 to 5.44 MUD.

(3) The decrease in pearlite interlamellar spacing from 158.9 to 110.3 nm is consistent with the expected trend associated with transformation undercooling and carbon diffusion; however, the actual pearlite transformation temperatures were not directly measured.

(4) The regional variations in strength and hardness were associated with smaller EBSD orientation-domain size and reduced pearlite interlamellar spacing; nanoscale V-rich precipitates may provide an additional contribution to strengthening. The ultimate tensile strength increased from 1130.7 to 1180.6 MPa, while the hardness increased from approximately 33 to 36 HRC.

Author Contributions: Writing—review and editing and funding acquisition, S.Y.; writing—original draft preparation, J.N.; investigation and data curation, H.L.; software, Z.Y.; methodology, F.D. All authors have read and agreed to the published version of the manuscript.

Funding: This research was funded by the National Natural Science Foundation of China (Grant No. 52271030).

Data Availability Statement: The raw data supporting the conclusions of this article will be made available by the authors on request.

Conflicts of Interest: Junjie Nie is employee of China Academy of Machinery Zhengzhou Research Institute of Mechanical Engineering Co., Ltd. All authors declare that the research was conducted in the absence of any commercial or financial relationships that could be construed as a potential conflict of interest.

References

1. Fei, J.; Qi, H.; Yuan, B.; Wan, M.; Zhang, L. Influences of Pearlite Interlamellar Spacing on Wear and Rolling Contact Fatigue Behaviors of Pearlitic Rails on Field Tracks. *Lubricants* **2026**, *14*, 267. [CrossRef]
2. Wang, X.; Xu, D.; Liu, G.; Liu, H. Experimental Study on Fatigue Performance of Steel Used in U75V Rails. *Materials* **2025**, *18*, 4706. [CrossRef]
3. Zhao, X.; Fan, Y.; Liu, Y.; Wang, H.; Dong, P. Evaluation of fatigue fracture mechanism in a flash butt welding joint of a U75V type steel for railroad applications. *Eng. Fail. Anal.* **2015**, *55*, 26–38. [CrossRef]
4. Li, Y.D.; Liu, C.B.; Xu, N.; Wu, X.F.; Guo, W.M.; Shi, J.B. A failure study of the railway rail serviced for heavy cargo trains. *Case Stud. Eng. Fail. Anal.* **2013**, *1*, 243–248. [CrossRef]
5. Yu, S.; Wang, Y.; Zhang, Z. Monitoring process parameters and predicting rail steel welded joint microstructure and mechanical property of three-wire fusion nozzle electroslag welding. *Weld. World* **2025**, *69*, 1229–1240. [CrossRef]
6. Su, Y.; Li, W.; Wang, X.; Ma, T.; Ma, L.; Dou, X. The sensitivity analysis of microstructure and mechanical properties to welding parameters for linear friction welded rail steel joints. *Mater. Sci. Eng. A* **2019**, *764*, 138251. [CrossRef]
7. Gao, M.X.; Song, H.; Jia, H.; Jiang, J.J.; Tong, S.H.; Yuan, S.Y.; Wang, Z.Q. Study on the Temperature Changing Rules of U75V Rail in the Cooling Process. *Procedia Eng.* **2011**, *15*, 4579–4584. [CrossRef]
8. Hauser, D. Welding of railroad rails—A literature and industry survey. In *ASTM Special Technical Publications*; ASTM International: Washington, DC, USA, 1978.
9. Glushko, O.; Jarnot, J.; Vincely, C.; Holec, D.; Schnitzer, R. Mitigating the hardness loss due to divorced eutectoid transformation in pearlitic steels: Influence of the cooling rate and austenitization temperature. *Eur. J. Mater.* **2026**, *6*, 2727346. [CrossRef]
10. Muangjunburee, P.; Oo, H.Z.; Rahim, S.Z.A.; Srikarun, B. Abrasive wear performance of repair welds on R260 rail using different welding electrodes. *Results Eng.* **2025**, *26*, 104680. [CrossRef]
11. Kakizaki, T.; Koga, S.; Yamamoto, H.; Mikami, Y.; Ito, K.; Yamazaki, K.; Sasakura, S.; Watanabe, H. Microstructure features and formation mechanism in a newly developed electroslag welding. *Weld. World* **2022**, *66*, 313–324. [CrossRef]
12. Wang, Y.; Yu, S.; Zhou, L.; Liu, D. Improvement of microstructure and mechanical properties in U75V rail electroslag welding joints via temperature field control. *J. Mater. Res. Technol.* **2026**, *42*, 3297–3312. [CrossRef]
13. Khan, A.R.; Yu, S.; Wang, H.; Jiang, Y. Effect of cooling rate on microstructure and mechanical properties in the CGHAZ of electroslag welded pearlitic rail steel. *Metals* **2019**, *9*, 742. [CrossRef]
14. Lv, S.; Wu, H.H.; Wang, K.; Zhang, C.; Zhu, J.; Wang, S.; Wu, G.; Gao, J.; Yang, X.S.; Mao, X. Phase field simulation of eutectoid microstructure during austenite-pearlite phase transformation. *J. Mater. Res. Technol.* **2023**, *26*, 8922–8933. [CrossRef]
15. Zhang, X.; Liao, T.; Liu, X.; Shen, X.; Tian, R.; Yang, X.Y.; Guo, B.; Lv, Q.; Gou, G.; Huang, X. Effect of normalisation on the microstructure and wear resistance of U75V rail welded joints in desert service environments. *J. Mater. Res. Technol.* **2025**, *35*, 2337–2345. [CrossRef]
16. Rodrigues, K.F.; de Faria, G.L. Characterization and Prediction of Continuous Cooling Transformations in Rail Steels. *Mater. Res.* **2021**, *24*, e20200519. [CrossRef]
17. Wang, Y.; Yu, S.; Zhou, L.; Liu, D. The influence of Ti on the microstructure and mechanical properties of U75V rail steel welds in three-wire fusion nozzle electroslag welding. *J. Mater. Res. Technol.* **2025**, *38*, 3564–3577. [CrossRef]
18. Lin, S.; Borgenstam, A.; Stark, A.; Hedström, P. Effect of Si on bainitic transformation kinetics in steels explained by carbon partitioning, carbide formation, dislocation densities, and thermodynamic conditions. *Mater. Charact.* **2022**, *185*, 111774. [CrossRef]
19. Feng, L.; Hu, F.; Zhou, W.; Ke, R.; Zhang, G.; Wu, K.; Qiao, W. Influences of Alloying Elements on Continuous Cooling Phase Transformation and Microstructures of Extremely Fine Pearlite. *Metals* **2019**, *9*, 70. [CrossRef]
20. *GB/T 2585-2021*; Hot-Rolled Steel Rails for Railway. Standardization Administration of China; Standards Press of China: Beijing, China, 2021.
21. *JB/T 6967-1993*; General Technical Conditions for Electroslag Welding. Ministry of Machinery Industry of the People's Republic of China; China Machine Press: Beijing, China, 1994.
22. Sun, X.; Liu, H.; Song, W.; Villecco, F. Modeling of Eddy Current Welding of Rail: Three-Dimensional Simulation. *Entropy* **2020**, *22*, 947. [CrossRef]

23. Deng, D.; Kiyoshima, S. Numerical simulation of welding temperature field, residual stress and deformation induced by electro slag welding. *Comput. Mater. Sci.* **2012**, *62*, 23–34. [CrossRef]
24. Xu, R.; Zhang, M.; Gao, Z.; Zhao, G.; Ding, W.; Wang, S.; Zhang, P.; Liu, X.; Li, J. Temperature field calculation of rail flash welding. *High-Speed Railw.* **2024**, *2*, 116–121. [CrossRef]
25. DebRoy, T.; Szekely, J.; Eagar, T.W. Temperature profiles, the size of the heat-affected zone and dilution in electroslag welding. *Mater. Sci. Eng.* **1982**, *56*, 181–193. [CrossRef]
26. Shome, M. Effect of heat-input on austenite grain size in the heat-affected zone of HSLA-100 steel. *Mater. Sci. Eng. A* **2007**, *445–446*, 454–460. [CrossRef]
27. Pickering, F.B.; Garbarz, B. The effect of transformation temperature and prior austenite grain size on the pearlite colony size in vanadium treated pearlitic steels. *Scr. Metall.* **1987**, *21*, 249–253. [CrossRef]
28. Li, S.; Gao, J.; Han, Z.; Feng, H.; Chen, C.; Zhao, H.; Wang, S.; Wang, K.; Wu, G.; Wu, H.; et al. Enhancing strength and toughness in a pearlitic rail steel via multi-alloying and accelerated cooling. *Mater. Sci. Eng. A* **2024**, *918*, 147444. [CrossRef]
29. Mukherjee, M.; Saha, S.; Pal, T.K.; Kanjilal, P. Influence of modes of metal transfer on grain structure and direction of grain growth in low nickel austenitic stainless steel weld metals. *Mater. Charact.* **2015**, *102*, 9–18. [CrossRef]
30. Karmakar, A.; Mukherjee, S.; Kundu, S.; Srivastava, D.; Mitra, R.; Chakrabarti, D. Effect of composition and isothermal holding temperature on the precipitation hardening in Vanadium-microalloyed steels. *Mater. Charact.* **2017**, *132*, 31–40. [CrossRef]
31. Bepari, M.M.A. Effects of precipitates on strength and toughness of vanadium structural steels. *Mater. Sci. Technol.* **1990**, *6*, 338–348. [CrossRef]
32. Kavishe, F.P.L.; Baker, T.J. Effect of prior austenite grain size and pearlite interlamellar spacing on strength and fracture toughness of a eutectoid rail steel. *Mater. Sci. Technol.* **1986**, *2*, 816–822. [CrossRef]
33. Elwazri, A.M.; Wanjara, P.; Yue, S. The effect of microstructural characteristics of pearlite on the mechanical properties of hypereutectoid steel. *Mater. Sci. Eng. A* **2005**, *404*, 91–98. [CrossRef]
34. Vermeij, T.; Hoefnagels, J.P.M. Plasticity, localization, and damage in ferritic-pearlitic steel studied by nanoscale digital image correlation. *Scr. Mater.* **2022**, *208*, 114327. [CrossRef]
35. Caballero, F.G.; Capdevila, C.; García de Andrés, C. Modeling of the interlamellar spacing of isothermally formed pearlite in a eutectoid steel. *Scr. Mater.* **2000**, *42*, 537–542. [CrossRef]
36. Nakajima, K.; Apel, M.; Steinbach, I. The role of carbon diffusion in ferrite on the kinetics of cooperative growth of pearlite: A multi-phase field study. *Acta Mater.* **2006**, *54*, 3665–3672. [CrossRef]
37. Aranda, M.M.; Kim, B.N.; Rementeria, R.; Capdevila, C.; García de Andrés, C. Effect of Prior Austenite Grain Size on Pearlite Transformation in a Hypoeutectoid Fe-C-Mn Steel. *Metall. Mater. Trans. A* **2014**, *45*, 1778–1786. [CrossRef]
38. Zhang, F.; Zhao, Y.; Tan, Y.; Ji, X.; Xiang, S. Study on the Nucleation and Growth of Pearlite Colony and Impact Toughness of Eutectoid Steel. *Metals* **2019**, *9*, 1133. [CrossRef]
39. Hall, E.O. The Deformation and Ageing of Mild Steel: III Discussion of Results. *Proc. Phys. Soc. Sect. B* **1951**, *64*, 747–753. [CrossRef]
40. Petch, N.J. The Cleavage Strength of Polycrystals. *J. Iron Steel Inst.* **1953**, *174*, 25–28.
41. Yahyaoui, H.; Sidhom, H.; Braham, C.; Baczmański, A. Effect of interlamellar spacing on the elastoplastic behavior of C70 pearlitic steel: Experimental results and self-consistent modeling. *Mater. Des.* **2014**, *55*, 888–897. [CrossRef]
42. Hyzak, J.M.; Bernstein, I.M. The role of microstructure on the strength and toughness of fully pearlitic steels. *Metall. Trans. A* **1976**, *7*, 1217–1224. [CrossRef]

Disclaimer/Publisher's Note: The statements, opinions and data contained in all publications are solely those of the individual author(s) and contributor(s) and not of MDPI and/or the editor(s). MDPI and/or the editor(s) disclaim responsibility for any injury to people or property resulting from any ideas, methods, instructions or products referred to in the content.